*Article*

# A Novel Magnetic Actuation Scheme to Disaggregate Nanoparticles and Enhance Passage across the Blood–brain Barrier

**Ali Kafash Hoshiar [1], Tuan-Anh Le[2], Faiz Ul Amin[3], Myeong Ok Kim[3], and Jungwon Yoon [2]\***

[1] Faculty of Industrial and Mechanical Engineering, Islamic Azad University, Qazvin Branch, Qazvin, Iran, 34199-15195; Hoshiar@Qiau.ac.ir

[2] School of Integrated Technology, Gwangju Institute of Science and Technology, 123 Cheomdangwagi-ro, Buk-gu, Gwangju, Korea, 61005; tuananhtbbk@gmail.com

[3] Department of Biology and Applied Life Science, Gyeongsang National University, Jinju 660-701, Republic of Korea.;faizgnu@gmail.com (F.U.A); mokim@gnu.ac.kr (M.O.K)

\* Correspondence: jyoon@gist.ac.kr; Tel.: +82-62-715-5332

**Abstract:** The blood–brain barrier (BBB) hinders drug delivery to the brain. Despite various efforts to develop preprogramed actuation schemes for magnetic drug delivery, the unmodeled aggregation phenomenon limits drug delivery performance. This paper proposes a novel scheme with an aggregation model for a feed-forward magnetic actuation design. A simulation platform for aggregated particle delivery is developed and an actuation scheme is proposed to deliver aggregated magnetic nanoparticles (MNPs) using a discontinuous asymmetrical magnetic actuation. The experimental results with a Y-shaped channel indicated the success of the proposed scheme in steering and disaggregation. The delivery performance of the developed scheme was examined using a realistic, three-dimensional (3D) vessel simulation. Furthermore, the proposed scheme enhanced the transport and uptake of MNPs across the BBB in mice. The scheme presented here facilitates passage of particles across the BBB to the brain using an electromagnetic actuation scheme.

**Keywords:** Asymmetrical discontinuous field function, blood–brain barrier (BBB), magnetic drug delivery, magnetic nanoparticles, aggregation.

## 1. Introduction

In recent years, many nanorobotic systems have emerged for studies in biology [1–5], and developments in magnetic nanoparticles (MNPs) for biomedical applications have considerably exceeded expectations, as the versatile natural properties of MNPs facilitate biological applications such as drug delivery. Functionalized MNPs showed encouraging results in crossing the blood–brain barrier (BBB) [6,7]. Magnetic drug delivery can be used to increase drug uptake. In magnetic drug delivery (MDD), the drug is added to MNPs, which are injected into a blood vessel and circulate throughout the vasculature. An external magnetic field is next applied to achieve the optimal concentration of drug-loaded particles in the desired location [8,9].

MNPs have myriad applications as therapeutic and diagnostic agents. Recent studies of MNPs for MDD applications revealed their magnetic properties, biocompatibility, and toxicity [10]. MNPs have unique optical properties suitable for *in vivo* tracking and are capable of delivering drugs to brain cells [11]. Drug-conjugated MNPs are used for drug delivery [12,13] by applying an external magnetic field to a location of interest in the body.

29    Although drug delivery using a magnetic field has been around for decades [14], recent
30 developments made MNPs feasible for MDD. Studies on MDD focused on simulation and analysis of
31 the captured and retained particles using a constant external magnetic field. Numerical simulations
32 of blood flow and MNP distribution in a realistic brain vessel demonstrated that MDD significantly
33 increases particle capture [15]. Particle size, type and coating, which influence capture efficiency,
34 were studied in a computer simulation; particle retention decreased with increasing particle size [16].
35 However, particle sticking and aggregation were neglected in these simulations.
36    The concentration of MNPs under a constant magnetic field using a Y-shaped bifurcation has
37 been reported [17], and the aggregation of MNPs under a constant magnetic field has been examined
38 experimentally [18]. MNPs reportedly stick to vessel walls due to the low flow velocity [19]. Steering
39 of aggregated microparticles under a constant magnetic field in a Y-shaped channel resulted in the
40 accumulation of aggregates at the bifurcation [20]. A constant magnetic field is used to facilitate
41 passage across the BBB, which is mediated by endocytosis [21]. Real-time *in vivo* monitoring of drug
42 delivery using a constant magnetic field has been evaluated [22]. Moreover, after crossing the BBB
43 under the guidance of a uniform magnetic field, MNPs formed rod-shaped aggregates [23]. Although
44 in [18] sticking was reduced by changing the shape of the magnet, this is not a general solution
45 to sticking; indeed, despite successful passage across the BBB, sticking and aggregation were not
46 considered in [21].
47    We resolved particle sticking by simulating intentional changes in the magnetic field direction
48 [24]. The use of dynamic magnetic actuation (change in field direction) to reduce aggregation was
49 investigated in [25]. The findings in [26] showed that dynamic actuation with a pulse-shaped
50 magnetic field using permanent magnets improves passage through the BBB. To evaluate drug uptake
51 in the brain, time-varying dynamic magnetic actuation was evaluated in the brains of mice. In the
52 absence of a magnetic field, no nanoparticles (NPs) were found in the brain [27]. Using magnetic
53 field function, however, the rate of BBB passage and drug uptake increased significantly [27]. Despite
54 the acceptable performance *in vivo*, aggregation in a magnetic field was not modeled. To improve
55 dynamic actuation for BBB passage, particle aggregation should be modeled.
56    Cluster structure and aggregation were previously evaluated numerically in a two-dimensional
57 (2D) platform [28]. Vartholomeos and Mavroidis developed a simulation platform to aggregate MNPs
58 and increase the magnetic force in a simulation [29]. A computational platform was designed to assess
59 the guidance of aggregated particles under a constant magnetic field [30]. A simulation platform was
60 also developed to deliver aggregated particles under a dynamic magnetic field in a Y-shaped channel
61 [31]. However, a discontinuous magnetic actuation scheme that minimizes aggregation and increases
62 the rate of BBB passage has not been reported to date.
63    In this scheme, the NPs are injected into a vein and circulate through the vasculature. We
64 propose a novel discontinuous asymmetrical dynamic actuation scheme to change the magnetic field
65 and deliver MNPs. This method is aimed at facilitating BBB passage by minimizing aggregation
66 through insertion of a deactivation time ($T_{dis}$) between each cycle, as shown in Fig. 1. A
67 simulation platform is utilized to assess delivery of aggregated particles under the dynamic actuation
68 scheme. A discontinuous asymmetrical field function (DAFF (t)), which generates a discontinuous
69 unequal alternating magnetic gradient, enables changes in field direction to guide MNPs. The
70 functionality and performance of this approach in terms of particle sticking were evaluated in a
71 realistic three-dimensional (3D) simulation of a vessel. The proposed design improved BBB passage
72 by MNPs and decreased the size of aggregates after BBB passage.
73    This paper is organized as follows: in section 2, the computational model for particle guidance is
74 developed, the concept and design of the DAFF are introduced, and the DAFF is studied for steering
75 MNPs in a Y-shaped channel. In addition, the effects of DAFF on particle sticking are investigated in
76 a realistic 3D vessel simulation. Finally, *in vivo* evaluation of passage through the BBB by MNPs is
77 presented. Section 3 presents the setup of the experiments. We concluded that the proposed scheme
78 increases the rate of BBB passage by MNPs.
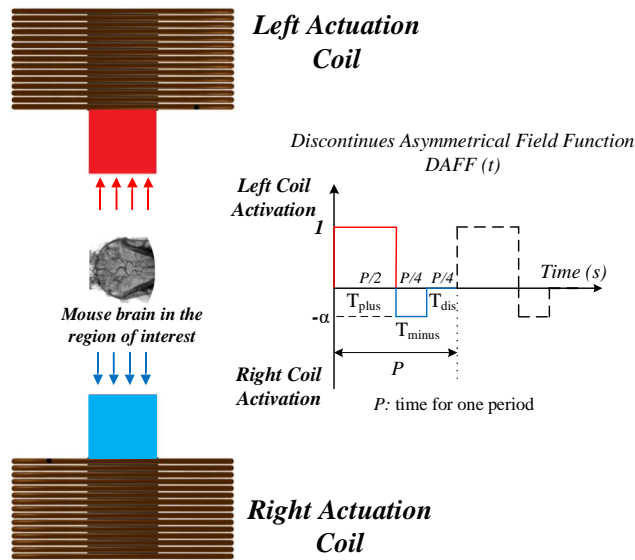
**Figure 1.** Schematic of the discontinuous magnetic actuation system for drug delivery and blood–brain barrier (BBB) passage using the proposed discontinuous asymmetrical field function (DAFF).

## 2. Results and Discussion

### 2.1. Governing Dynamic Forces in MDD

To fully understand MNP aggregation, the forces governing MNP steering are modeled in this section. Many parameters presented in this section will be used throughout the manuscript; any changes in them will be stated. The forces depicted in Fig. 2 were considered and the Newtonian dynamic model is used:

$$m_i \frac{d\mathbf{v}_i}{dt} = \mathbf{F}_{MF} + \mathbf{F}_{\text{dip}} + \mathbf{F}_{\text{drag}} + \mathbf{F}_{CA} + \mathbf{F}_m \tag{1}$$

where index $i$ indicates particle $i$, $m_i$ is the particle mass, $v_i$ is the particle velocity, $F_{MF}$ is the magnetic force, $F_{dip}$ is the dipole force, $F_{drag}$ is the hydrodynamic drag force, $F_m$ is the gravitational force
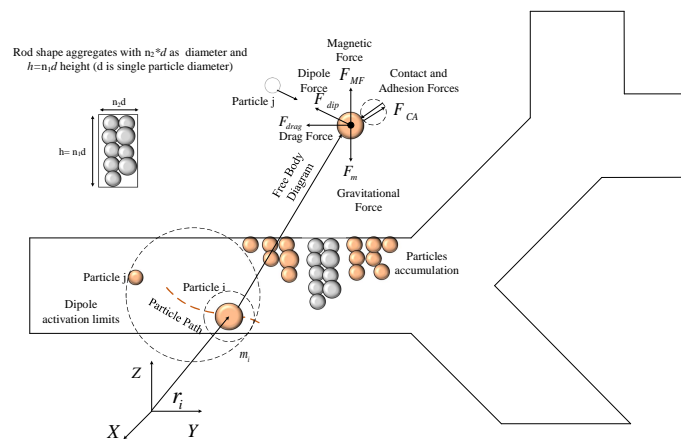


**Figure 2.** T2 A particle *i* inside the vessel is considered; the effective forces are shown in the free-body diagram and the geometry of the rod-shape aggregates is illustrated.

87 (gravity and buoyancy), and $F_{CA}$ is the contact-adhesive force. To use Newtonian mechanics, particles
88 are considered to be large enough to exclude the effect of Brownian motion [29,32].

89 The magnetic force is the actuation force used for steering. MNPs exhibit almost hysteresis-free
90 behavior. If the permeability in medium satisfies the relation $\mu_1 = \mu_0$ ($\mu_0$ is the permeability of the
91 free space) and, considering the magnetic polarization ($M$) as a function of magnetic intensity ($H$),
92 which has a finite limit of $M_{sat}$, and the magnetic field is considered large enough to create the finite
93 value $M_{sat}$, and $V$ is considered to be the volume of the rod-shaped aggregates, then the magnetic
94 force can be modeled as:

$$F_{MF} = V\mu_1 M_{\text{sat}}.\nabla H_f \tag{2}$$

95 The rod-shaped aggregates have a diameter of $n_2 d$ and a height of $n_1 d$, with $d$ being the diameter
96 of a single MNP. $n_1$ and $n_2$ are the number of particles in the aggregate (the rod-shaped aggregates
97 are shown in Fig. 2). The aggregate volume is represented as $\frac{\pi}{4} n_1 n_2^2 d^3$.

98 $F_{dip}$ is the dipole force, which plays a major role in keeping the particles together. The dipole
99 force is modeled as:

$$F_{dip} = \frac{3\mu_1 m_i m_j}{4\pi r_{ij}^4}(r_{ij}(m_i.m_j)$$

$$+m_i(r_{ij}.m_j) + m_j(r_{ij}.m_i) - 5r_{ji}(r_{ji}.m_i)(r_{ji}.m_j) \tag{3}$$

100 where $\mu_1$ is the magnetic permeability of the medium, $m_i$ and $m_j$ are the magnetic moments of the $i^{th}$
101 and $j^{th}$ particles and $r_{ij}$ is the distance between particles.

During aggregation, the dipole force has two main effects: an initial negligible contribution to
magnetic intensity ($H$), and a major influence on particle-particle sticking. To model the magnetic
moment, a system of coupled equations must be solved [29,30]. The total magnetic intensity for the
particle of interest is given as:

$$H = H_{\text{ext}} + \sum_j^N H_{\text{dip}} \tag{4}$$

102 where $H_{ext}$ is the external magnetic intensity, and *sum* is the accumulated effect of other particles.

The drag (hydrodynamic) force on the particles based on Stokes law is:

$$F_{\text{drag}} = -3\pi\eta d(v_p - v_f) \tag{5}$$

103 where $v_p$ and $v_f$ are the particle and fluid velocities, respectively, $d$ is the particle diameter, and $\eta$ is
104 the fluid viscosity.

105 The gravitational force is yielded by gravity and buoyancy forces as follows:

$$F_m = \frac{1}{6}\pi d^3(\rho_p - \rho_b)G \tag{6}$$

106 where $d$ is the particle diameter, $\rho_p$ and $\rho_b$ are the particle and blood densities, respectively.

The contact-adhesive forces are generated by particle-particle or particle-surface collisions. The
Hertzian contact model can be expressed as:

$$F_c = k\delta^{\frac{3}{2}} \overset{\text{If}}{\longleftrightarrow} P_{dis} < R_i + R_j \tag{7}$$

107 where $P_{dis}$ is the particle-particle distance, $R_i$ is the $i^{th}$ particle radius, $R_j$ is the $j^{th}$ particle radius, $k$ is
108 the spring constant, and $\delta$ is deformation.

The adhesive force is also modeled as:

$$F_{Ad} = \tau\pi\left(\frac{3F_c d}{8E^*}\right)^{\frac{2}{3}} \tag{8}$$
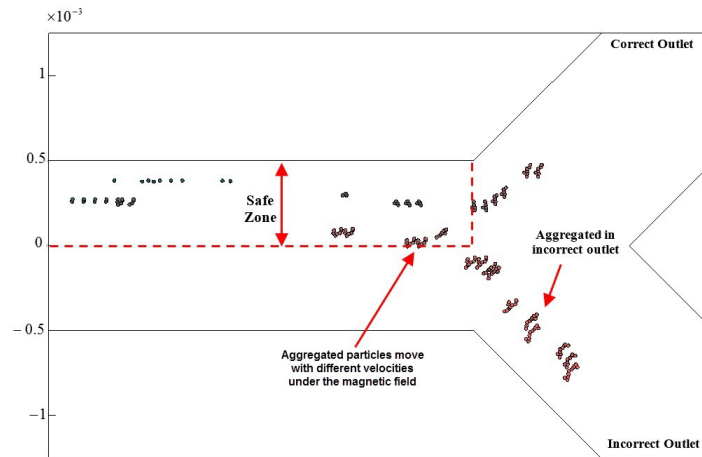
**Figure 3.** Steering aggregated magnetic nanoparticles (MNPs) in a Y-shaped channel using magnetic actuation.

where $\tau$ is the adhesive energy (a constant parameter), $d$ is the equal diameter($d = 2 * \frac{R_1 R_2}{R_1 + R_2}$), $F_c$ is the contact force, and $E^*$ is the equal elasticity module. The opposite nature of the contact force (separation) and adhesion force (connection) creates the contact adhesive force, which is represented as:

$$F_{CA} = F_{Ad} + F_c \tag{9}$$

The trajectories of the MNPs can be determined by incorporating the forces in Eq. 1.

*2.2. Simulation platform for steering aggregated MNPs in bifurcations*

A Y-shaped channel that resembles the bifurcation is used in the simulation. The Y-shaped channel consists of one inlet and two outlets of constant diameter. A steady creeping flow enters through the inlet and exits via the outlets. Aggregation is considered to occur near the inner boundary of the vessel. Initially, the particles attract each other due to dipole effects. The contact-adhesive force balances this effect and mediates MNP aggregation. The magnetic force acts as a body force and moves the particle toward the direction of application; the drag force resists this movement. These forces are incorporated into the governing dynamic (Eq. 1), and a system of ordinary differential equations (ODEs) is formed.

In this simulation, 225 particles (800 nm diameter) were used and a system of 900 ODE equations is solved at each time step. The ODE system is numerically solved using the Runge Kutta method. The magnetic and drag forces govern the dynamics of the movement of particles inside the vessel. The magnitude of the magnetic forces varies with the number of aggregated particles in a rod. Therefore, particle velocity varies according to aggregate size. The number of particles in aggregates determines the velocity; therefore, aggregate size is used in the simulation to match the experimental data [31,33].

Fig. 3 shows a simulation of MNP aggregation within a Y-shaped channel. The rod-shaped aggregates move based on the magnetic actuation at different velocities, and reach the bifurcation. Using this simulation platform, which considers the physical parameters in Table 1, guidance can be evaluated by computing the number of particles that reach the correct outlet. It was assumed that particles that remain inside the safe zone will be guided to the correct outlet [33]. The safe zone is the distance between the vessel boundary of the correct outlet and the mid-vessel line (Fig. 3). A high percentage of particles reaching the correct outlet reflects the delivery performance of the MNPs by the magnetic field.

**Table 1.** Simulation Parameters.

| Parameter | value |
|---|---|
| Particle density | $6450 \, kg/m^3$ |
| Particle diameter | $800 \, nm$ |
| Blood density | $1050 \, kg/m^3$ |
| Blood viscosity | $0.004 \, Pa.s$ |
| Air relative permeability | $1 \, Dimensionless$ |
| Blood relative permeability | $1 \, Dimensionless$ |
| Blood temperature | $293.15 \, K$ |

133 2.2.1. The Influential Parameters in Targeting Performance

134 Three coefficients were introduced to investigate the effect of aggregation on guidance. The
135 guidance performance in a Y-shaped bifurcation depends on the vessel elongation ratio ($R_{ve}$) for the
136 vessel geometry, normal exit time ($T_c$) as an environmental condition, and the force factor ($R_f$) [24].
137 The normal exit time represented by $T_c$ shows the influence of vessel elongation and flow
138 velocity. This factor represents the minimum time needed for the aggregated particles to reach the
139 bifurcation point. In the vascular network, the blood-flow velocity varies between a few millimeters
140 per second in capillaries to a few centimeters per second in arteries [20]. The normal exit time is
141 shown in Eq. (10). The designed actuation should be robust to these changes and be able to safely
142 guide the particle to the desired outlet. To study this effect, the vessel nominal length is considered
143 to be 10 mm and the normal exit time varies based on the information in Table 2.

$$T_c = \left(\frac{L_v}{V_b}\right) \tag{10}$$

144 where $L_v$ is the vessel length and $V_b$ is the flow velocity.

145 The diameter and length of blood vessels vary; this is represented by the vessel elongation ratio
146 $R_{ve}$, which is considered to a dimensionless factor comprising the vessel length to diameter ratio. To
147 study this parameter, the vessel nominal length is considered to be 10 mm and the $R_{ve}$ is changed
148 based on the information in Table 2. The vessel elongation factor is:

$$R_{ve} = \left(\frac{L_v}{D_v}\right) \tag{11}$$

149 where $L_v$ is the vessel length and $D_v$ is the vessel diameter.

The magnetic actuation force is mainly affected by two parameters: the magnitude of the
magnetic field gradient and the particle size. To evaluate the effect of the actuation force, the force
factor is defined as:

$$R_f = \left(H_g d^3\right) \tag{12}$$

150 where $H_g$ is the magnetic gradient and $d$ is the particle diameter. The particle diameter is considered
151 to have a mean value of 800 nm and the force factor used in the simulations is presented in Table 2.

The ability of a constant-direction magnetic field to steer MNPs is reportedly limited by particles
sticking to the vessel. This can be solved by alternating the dynamic magnetic actuation [24]. A field

**Table 2.** Units for Magnetic Properties.

| Symbol | Quantity | unit |
|--------|----------|------|
| $L_v$ | *Vessel length* | 10 *mm* |
| $T_c$ | *Normal exit time* | 5 *s* |
| $R_{ve}$ | *Vessel elongation* | 20, 10, 6.6, 0.5 *Dimentionless* |
| $R_f$ | *Force Factor* | 0.3, 0.6, 0.9, 1.2, 1.5, 1.8 *pA.m* |

function ($FF(t)$), which is a unitless multiplier, is proposed to change the direction of the magnetic field by activating the coils sequentially [24]. ($FF(t)$) for all values of $t$ is defined as:

$$-1 \leq FF(t) \leq 1 \qquad (13)$$

Here, the minus sign indicates the right coil (direction of incorrect outlet) and the plus sign indicates the left coil (direction of the correct outlet) (Fig. 1). This function defines the magnetic field, and has two properties: the frequency (Hz) and duty ratio (dimensionless) of activation time. The ratio of the activation time for the coil in the direction of the correct outlet to the activation time for the coil in the direction of the incorrect outlet is considered to be 3 to 1. Different frequencies were considered for simulation of MNP guidance [24]. Using $FF(t)$, the alternating gradient field is defined as:

$$\nabla H_f = FF(t)\nabla H \qquad (14)$$

Consequently, the actuation force is designed as:

$$F_{MF} = FF(t)VM_{\text{sat}}.\nabla H \qquad (15)$$

The frequency of the $FF(t)$ (Fig. 4 A) is considered to be 0.5 Hz, which is the best frequency suggested in [24]. However, the previous simulation did not consider the effects of the aggregation of MNPs within the magnetic field. A previously developed computational platform (Fig. 3) with aggregation modeling is used to study the guidance performance of aggregated MNPs. The number of particles reaching the correct outlet is calculated. The simulation results for aggregated particle guidance for all conditions in Table 2 are shown in Fig. 4.

The simulation results reveal two patterns of aggregated particle guidance with the $FF(t)$ (Fig. 4). By increasing the force factor (from $R_f = 0.3$ to 1.84), the success rate decreases in all cases. This is because when a higher force is applied, more particles leave the safe zone, and so guidance performance is decreased by the increase in the force factor. Therefore, an obvious trend of deterioration is observable for higher force factors. Moreover, a decrease in the vessel elongation factor results in an increase in the rate of successful guidance (Fig. 4). As the vessel elongation factor increases, the time needed for the particles to leave the safe zone increases. In this simulation, as the particles are considered to be aggregated, the normal exit time is not very influential.

As illustrated in Fig. 4, the delivery performance of FF (t) is sensitive to parameter changes. Moreover, the magnetic actuation ($FF(t)$) proposed in [24]) does not include the effects of aggregation and it generates large aggregates that hinder BBB crossing. Therefore, this paper uses a discontinuous asymmetrical field function to solve these issues.
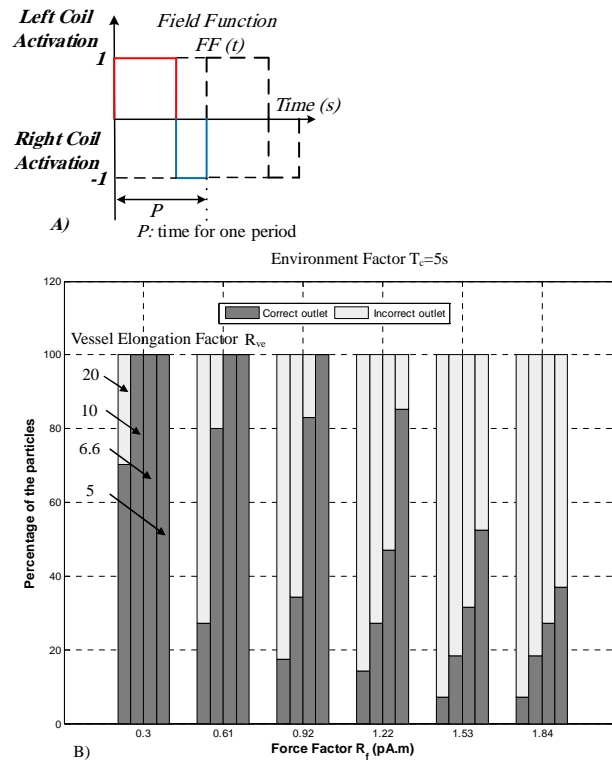
**Figure 4.** Simulation results for aggregated particle guidance. A) The field function for magnetic actuation, B) The delivery performance in a simulation of a Y-shaped vessel with $d_v$=1 mm, $L_v$=10 mm, $T_n$=5 s and field function (FF) (t) with 6A and duty cycle of 0.5 Hz.

177    2.2.2. The DAFF Design

The magnetic actuation scheme should be modified to reduce the adverse effects of aggregation. Therefore, we propose a DAFF to solve the aggregation issue. The DAFF is a unit-less multiplier with an asymmetric ratio of $\alpha$ and a magnitude of 1. The asymmetry ratio $\alpha$ is used to handle the aggregation effect and keep particles inside the safe zone (illustrated in Fig. 3). The DAFF also alternates the magnitude of the magnetic field sequentially. The $DAFF(t)$ is illustrated in Fig. 1 and for all values of *t* is defined as:

$$-\alpha \leq DAFF(t) \leq 1 \qquad \alpha \leq 1 \tag{16}$$

178    Here, the minus sign indicates the right coil (to the incorrect outlet) and the plus sign indicates
179    the left coil (to the correct outlet), as illustrated in Fig. 1.

180    In the absence of a magnetic force, the aggregated particles disaggregate due to the effects of
181    Brownian and drag forces. $T_{dis}$ is the time of discontinuity, in which both coils are inactive, considered
182    in the DAFF. The DAFF is defined by the activation ratio, discontinuity time ($T_{dis}$), frequency, and
183    asymmetry ratio ($\alpha$). DAFF has an activation ratio of 2 to 1 (for the coils) and the $T_{dis}$ is considered to
184    be equal to $T_{minus}$ (Fig. 1). The magnetic actuation force is introduced as:

$$F_{MF} = DAFF(t)VM_{\text{sat}}.\nabla H \tag{17}$$

185    The design objective here is to determine the magnitude of $\alpha$ (asymmetry ratio) and frequency
186    so that retains all particles inside the safe zone (Fig. 3). With the designed frequency and asymmetry
187    ratio, the particles will remain in the safe zone and can reach the correct outlet. Utilizing the
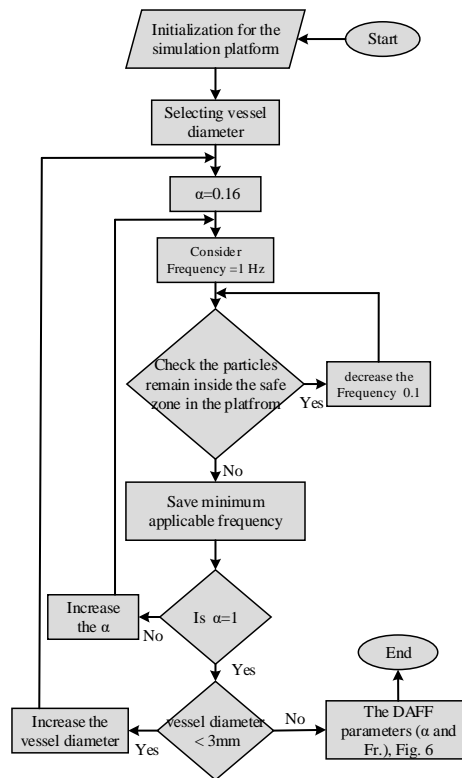
**Figure 5.** Flowchart of the frequency and $\alpha$ in the DAFF.

developed computational platform, the frequency and $\alpha$ are obtained to satisfy the design objective. The simulation flowchart for the discontinuous asymmetrical field function is shown in Fig. 5.

The current applied to the coils is 1, 2, 3, 4, 5, and 6 A [27]. Therefore, the asymmetry ratio $\alpha$ is considered to be 0.16, 0.33, 0.5, 0.66, 0.83, and 1, respectively. For a predefined bifurcation geometry with a diameter of 1 mm and length of 10 mm. Initially, the asymmetry ratio $\alpha$ is considered to be 0.16. In step 1, the actuation frequency is considered to be 1 Hz; then, the simulation platform is used to verify that all particles remain in the safe zone. If all particles remain in the safe zone, the frequency is decreased in 0.1 Hz increments. This cycle repeats unless the particles exit the safe zone. The minimum frequency that retains all aggregates inside the safe zone is obtained. In step 2, the asymmetry ratio $\alpha$ is increased; this process is repeated for different values of $\alpha$ (0.16, 0.33, 0.5, 0.66, 0.83, 1). In step 3, the vessel diameter is changed (2 and 3 mm), and the above process is repeated to determine the adequate frequency for each vessel diameter. The flowchart in Fig. 5 shows the process of determining the adequate frequency according to the asymmetry ratio in the DAFF and the vessel diameter.

Fig. 6 shows the relation between frequency and asymmetry ratio ($\alpha$), based on the flowchart in Fig. 5. Using the frequency and asymmetry ratio in Fig. 6 for DAFF, 100% guidance is achieved in the simulation. In addition, Fig. 6 indicates that, for lower asymmetry ratios ($\alpha$), a lower frequency can be applied, and the frequency increases with the rise in asymmetry ratio. A high frequency does not provide sufficient guidance and delivery performance [27,34]. Therefore, a low asymmetry ratio ($\alpha = 0.133$ and 0.33) and low frequency are used in this study.

*2.3. In vitro study of guidance of MNPs in a Y-shaped channel*

The experimental setup of the magnetic actuation platform is shown in Fig. 7. Electromagnetic actuators are designed to generate an adequate magnetic force to steer MNPs within the region of interest.
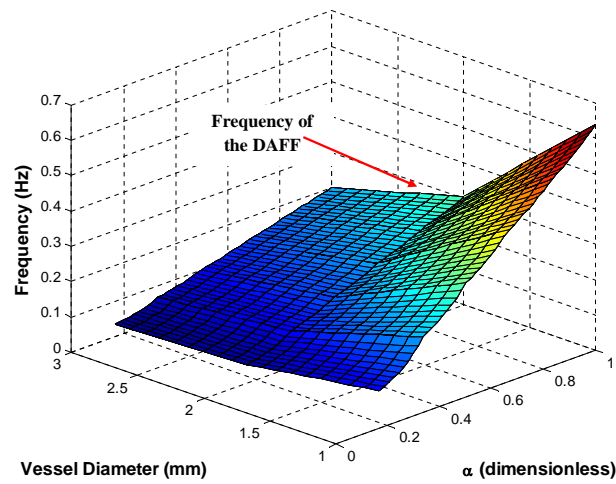
**Figure 6.** Frequency and asymmetry ratio $\alpha$ for high targeting performance in bifurcations of different diameters.

Fig. 8 shows the video image data for steering performance in FF and DAFF experiments, with the aim of providing a qualitative understanding of the different guidance behaviors of the FF and DAFF.
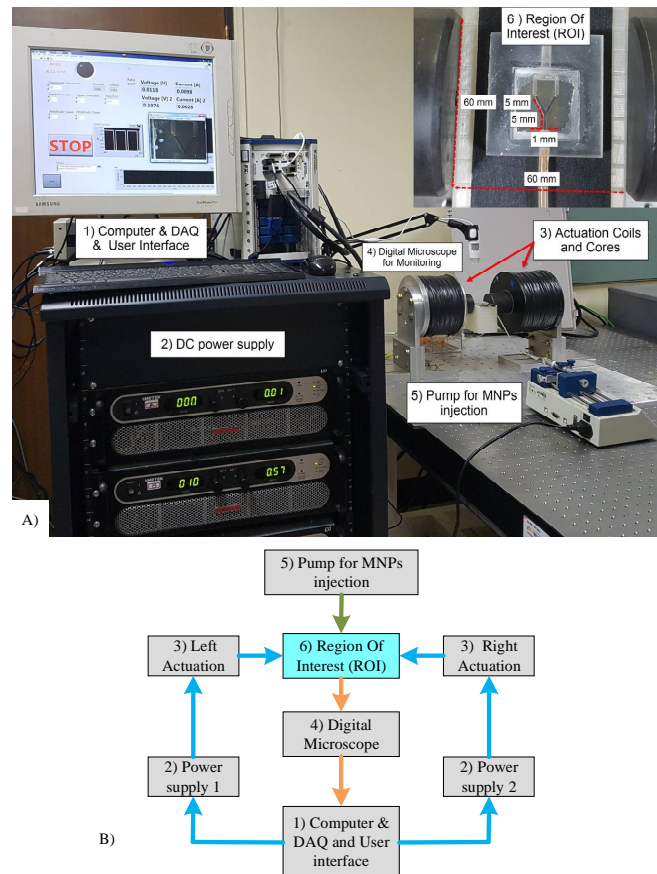
**Figure 7.** A) The electromagnetic actuator comprises two coils (5,000 turns and diameter of wire $d_w$ = 1.0 mm) with two cores to increase the magnetic field density (cobalt–iron alloy VACOFLUX 50, VACUUMSCHMELZE, German); the cores are 19.5 cm in length and 6 cm in diameter. Two power supplies (AMETEK SGA 600/17, 10 kW) are utilized to generate currents of up to 6 A (gradient field strength, 2.8 T/m) in the experiments. B) Schematic of the system.

Aggregated particles move through the channel, as shown in the supplementary video. The aggregates are oriented along the direction of the main magnetic field and move with the flow. In the absence of a magnetic field, particles flow similarly through both outlets. As the magnetic field with FF (0.5 Hz, 6 A) is applied, the aggregates move toward the correct outlet. A sudden change in the magnetic field results in aggregates entering the incorrect outlet (Fig. 8A) (supplemental video). Some aggregates accumulate at the branch of the channel and the boundary of the vessel; these form stationary aggregates.

Fig. 8B shows combined images obtained by averaging multiple video frames. These plots show aggregate accumulation during the steering experiments. The black parts of the images represent areas with the highest density of aggregates. Consistent with the simulation platform described in the previous section, these results represent the scenario in which the guidance performance of the aggregates fluctuates under FF and many particles enter the incorrect outlet. The formation of rod-shaped aggregates is also verified in this image. This phenomenon can be observed in Fig. 8B. Although a pulsed magnetic field reduced blood clotting compared with a constant magnetic field [20,30], stationary aggregates and aggregates entering the wrong outlet can lead to blood clotting. Therefore, the DAFF is proposed to prevent blood clotting caused by aggregates.

As the magnetic field with DAFF (0.144 Hz, $\alpha$ = 0.16) is applied, the aggregates move smoothly toward the correct outlet (Fig. 8C and supplemental video). The size of the aggregates is reduced significantly and stationary aggregates do not appear. Fig. 8D shows combined images. Black parts

234 of the images represent areas with the highest density of MNPs. These results confirm that the DAFF
235 improves guidance of the MNPs. The DAFF also reduced the size of aggregates.

236     Three differences between Fig. 8D and B are evident. The size of aggregates is reduced by use
237 of the DAFF for steering, aggregate fluctuations and entry to the incorrect outlet are minimized, and
238 there are no stationary aggregates in the incorrect outlet or at the boundary. Statistical analysis of
239 the images in Fig. 8B and D verifies these phenomena. Fig. 8E shows that accumulation of particles
240 in the correct outlet is twofold greater than that with the DAFF, which indicates that the aggregates
241 are larger. Moreover, particles are absent from the incorrect outlet with DAFF, but for FF, 8.5% of
242 the incorrect outlet is covered with MNPs. These results can be also seen in Fig. 8B and D and the
243 supplementary movie. By eliminating stationary aggregates and reducing aggregate size, the DAFF
244 reduces the risk of blood clotting.
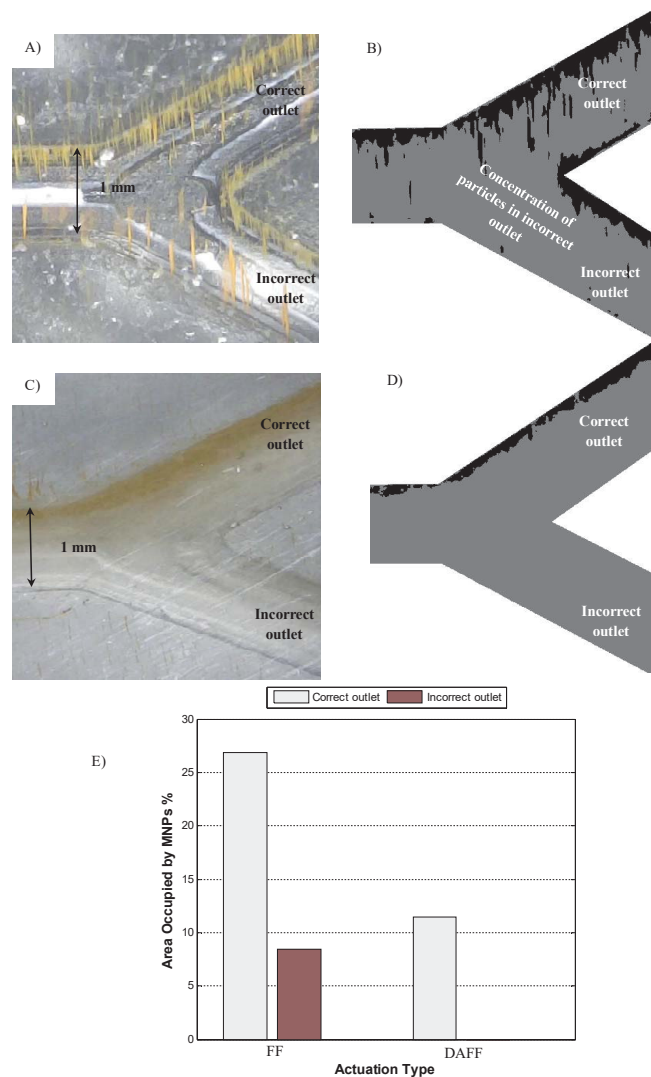


**Figure 8.** Video image analysis of the steering performance of a Y-shaped bifurcation. A) Raw image for a field function with (6A, 0.5 Hz). B) Combined images obtained from averaging several hundred frames (6A, 0.5 Hz). C) Raw image under asymmetrical discontinuous field function with (6A, 0.14 Hz and $\alpha$=0.16). D) Combined images obtained from averaging several hundred frames (6A, 0.14 Hz and $\alpha$=0.16). E) The percentage of accumulated NPs in the correct and incorrect outlets under FF and DAFF.
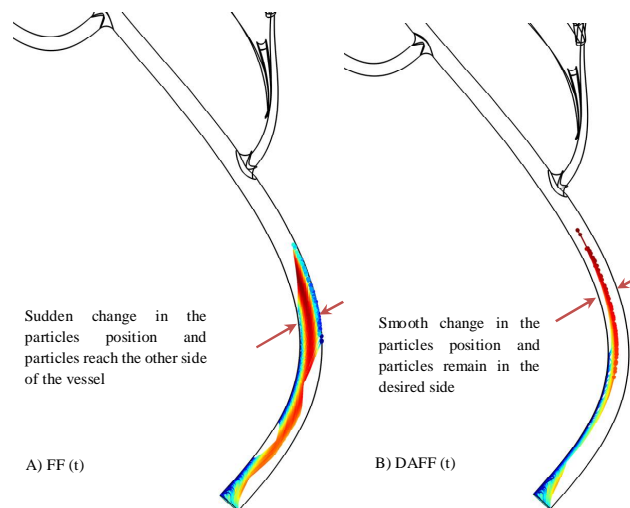
### 2.4. Realistic model simulation

To study the effects of the DAFF, a realistic 3D model was simulated in COMSOL. A special procedure was used to extract data from a magnetic resonance image (MRI) and create a computer-aided design (CAD) model [35]. The model was imported into COMSOL Multiphysics to assess particle trajectory. The realistic model consists of one inlet and six outlets with different diameters.

The average inlet velocity is selected based on a realistic blood velocity (10 mm/s) and the CFD module of COMSOL is used to obtain the velocity profiles in all channels. Other parameters are included in the simulation using the values in Table 1. The experimental studies in [36] suggested that 30% of MNPs are single particles and the magnetic actuation cannot guide them. In the simulation, 1,000 800-nm-diameter particles are realized uniformly in the inlet and their trajectories are recorded. To illustrate the aggregation effects, 30% of the particles are considered to be single particles, and 70% to be aggregates. Based on the aggregate geometry (Fig. 2), the equal diameter is considered to be:

$$d_{eq} = \frac{\pi}{2} n_1 n_2^2 d^3 \tag{18}$$

where $n_1$ and $n_2$ are simulation parameters for the geometry of rod-shaped aggregates (Fig. 2), and $d$ is the particle diameter. The equal radius for the aggregates is considered to match the experimental results in [31]. Guidance for delivering MNPs under the designed actuation is studied statistically, and the number of particles reaching each outlet is calculated using the trajectory module of COMSOL.

To assess differences in particle trajectories, the simulation time is initially considered to be $T_s$=7s for both $FF(t)$ and $DAFF(t)$; the trajectories are simulated in Fig. 9. Although FF resolves the sticking issue during movement of the MNPs, a sudden position change is observed and the particles reach the opposite side, which leads to MNP fluctuations within the vessel and limits guidance performance. By contrast, the DAFF yields smoother movements, which indicates stable steering performance.



Sudden change in the particles position and particles reach the other side of the vessel

A) FF (t)

Smooth change in the particles position and particles remain in the desired side

B) DAFF (t)

**Figure 9.** Particle tracking simulation of $T_s = 7s$ for A) a field function ($FF(t)$) and B) a discontinuous asymmetrical field function ($DAFF(t)$).

Fig. 10A shows the simulated vessel geometry. The effects of magnetic functions are studied in this simulation. Fig. 10B shows that in the absence of a magnetic field, only 13.7% of the particles reach the targeted outlet, and particles are distributed based on the drag force effects (Fig. 10B shows the delivery performance). Fig. 10C shows the effects of a constant magnetic field, which exacerbates the sticking issue; 73.7% of the particles remain within the vessel and only 3% reach the outlet. By contrast, although the field function (6 A and 0.5 Hz) resolves the sticking issue and 3.9% of the

particles remain in the vessel (Fig. 10D), the number of particles in the targeted outlet increases only slightly to 11.4%. In comparison, for DAFF with $\alpha$ = 0.166 and a frequency of 0.144 Hz (Fig. 10E), the number of particles reaching the targeted outlet increased significantly (72.2% for DAFF) due to the smooth movement of the particles in the vessel. By alternating the field direction, outlet 6 is also considered for delivery; using the same DAFF in this direction, 76.8% of the particles are delivered.
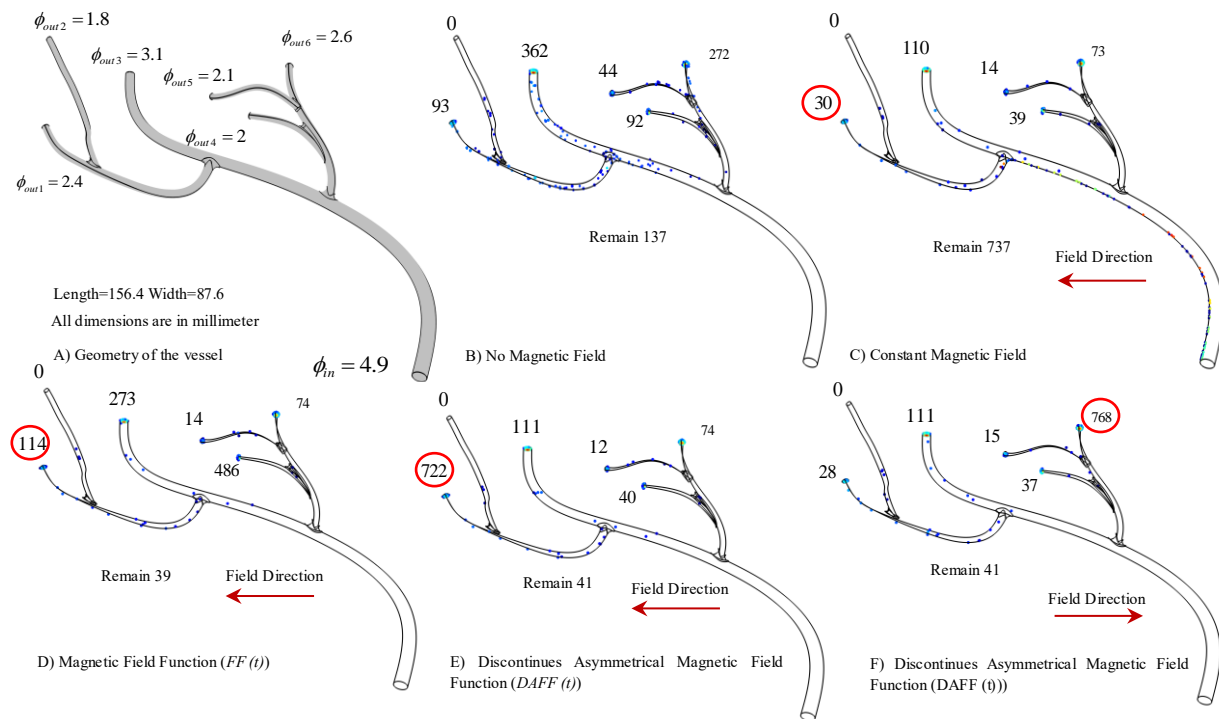


**Figure 10.** The simulation of the MNP distribution in a realistic vessel under the different designed actuation functions. The number close to each outlet is the number of particles reaching that outlet: A) the realistic vessel geometry; B) the distribution of particles under a drag force in the absence of a magnetic field; C) a constant magnetic field; D) the FF; and E) the discontinuous asymmetrical FF.

### 2.5. Passage of the BBB

[37] confirmed the passage of NPs through blood vessels *in vivo* under a magnetic force. They show the BBB being crossed under a magnetic field inside vessels using atomic force microscopy (AFM). In this section, we show the particles after crossing the BBB under a magnetic field, which is in agreement with the results in [27,37].

Superparamagnetic iron oxide (SPIO) NPs satisfy the conventional cytotoxicity assessment, but once they are exposed to a static magnetic field their aggregation adversely affects their toxicity [38]. However, the coating reduces both the aggregation and toxicity of the NPs [39]. One of the main objectives of our paper was to reduce aggregation by using discontinuous asymmetrical magnetic actuation. Therefore, the combined effects of coating and DAFF have a positive effect on reducing toxicity.

Pulse-shaped magnetic fields enhance passage through the BBB [26]. However, the functionality is limited by unmodeled aggregation. The *in vitro* experiments in this paper showed the destructive effect of aggregation. Therefore, the DAFF is designed to disaggregate the MNPs and improve the delivery of NPs to the brain. To examine the effects of the proposed actuation scheme *in vivo*, several experiments were conducted using the experimental setup in Fig. 7 and test subjects were positioned inside the ROI (Fig. 1).

Fluorescent MNPs (FMNPs) were injected into mice via the tail vein and then exposed to magnetic field conditions for 10 mins. FMNP uptake in the brain was verified using confocal microscopy. Fig. 11 shows confocal microscopy images of mouse brains under DAFF (Fig. 11(A)), FF (Fig. 11(B)), and no magnetic field (Fig. 11(C)). We first analyzed the brains of mice in the absence of a magnetic field; no accumulation of FMNPs in the brain was observed (Fig. 11C). FMNP uptake and transport were significantly higher for all magnetic actuations (Fig. 11D 1-2) compared with the control group (Fig. 11D 3). Interestingly, compared with the best condition for FF, which was introduced in [27], the rate of particle transport across the BBB was increased significantly (1.5-fold) under condition 1 (DAFF, $\alpha = 0.16$), which showed that a discontinuous asymmetrical field function improved FMNP uptake and transport to the mouse brain compared with FF (Fig. 11D).

Fig. 12 shows the average size of MNPs in the brain after crossing the BBB. Fig. 12A and B illustrates particle detection and categorization after BBB crossing under DAFF and FF. Fig. 12B shows the average size of aggregates. Aggregates in condition 2 (FF) had a larger average size than those in condition 1 (DAFF). Therefore, DAFF can be used to enhance the transport of MNPs across the BBB, while resulting in markedly smaller aggregates. More importantly, our results demonstrate the importance of exploring the effects of variation in the magnetic field in the context of *in vivo* drug delivery applications.
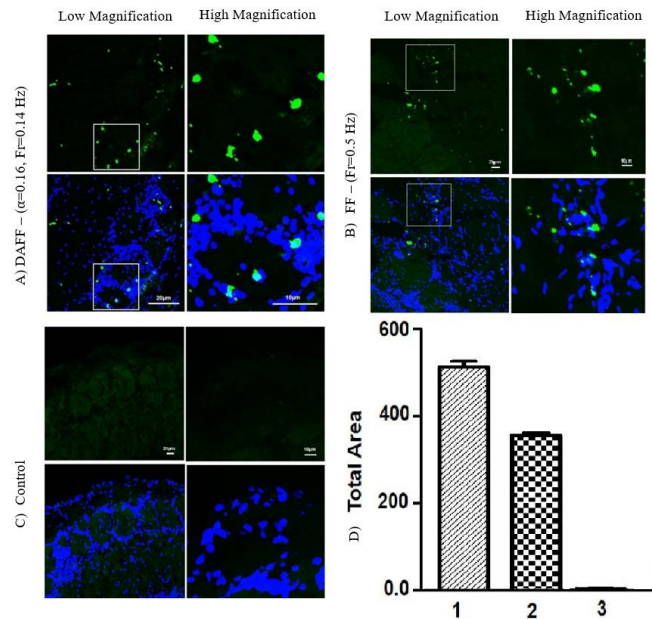


**Figure 11.** Confocal microscopy images of brain tissue samples: A) $DAFF(t)$, 6 A, $\alpha = 0.16$, 0.144 Hz, B) $FF(t)$, 6 A, 0.5 Hz [27], C) control, and D) MNP accumulation. Data are the mean $\pm$ SEM of triplicate experiments ($n = 3$), 1) $DAFF(t)$, 6 A, $\alpha = 0.16$, 0.144 Hz, 2) $FF(t)$, 6 A, 0.5 Hz, and 3) control.
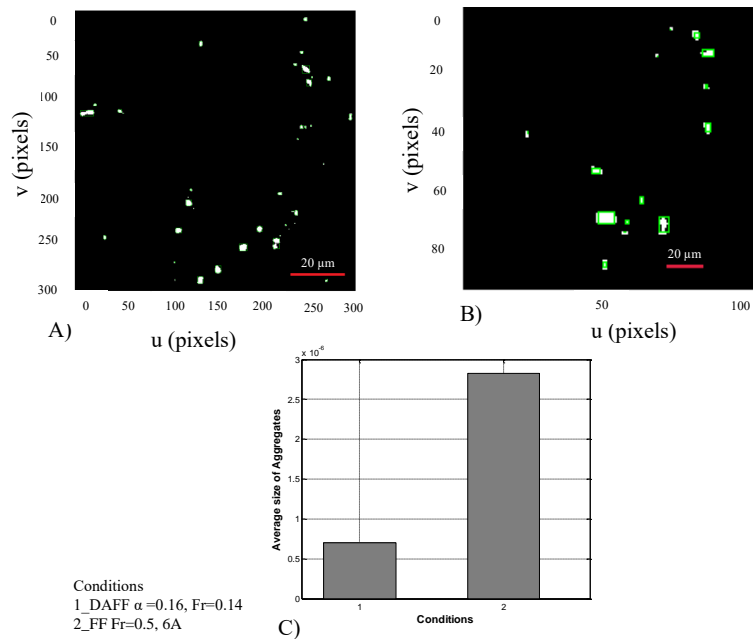
**Figure 12.** Aggregation of fluorescent MNPs (FMNPs) after crossing the BBB with different magnetic FFs. Aggregates under A) discontinuous asymmetrical field function (DAFF) and B) FF. C) MNP accumulation under 1) $DAFF(t)$, 6 A, $\alpha$ = 0.16, 0.144 Hz and 2) $FF(t)$, 6 A, 0.5 Hz.

## 3. Experimental Section

### 3.1. System setup

The region of interest is 60 mm in diameter at the center of the actuation system. The electromagnetic actuator comprises two coils (5,000 turns, wire diameter $d_w$ = 1.0 mm) with two cores to increase the magnetic field intensity (cobalt–iron alloy VACOFLUX 50; VACUUMSCHMELZE, Hanau, Germany); the cores are 19.5 cm in length and 6 cm in diameter. Two power supplies (SGA 600/17, 10 kW; AMETEK, Berwyn, PA, USA) are used to generate currents of up to 17 A (maximum gradient field strength, 7.9 T/m). In the experiments, a maximum current of 6 A (2.8 T/m) is used [34]. An NI PXIe 8135 is used to control the coils and a digital microscope is used to monitor the MNPs.

### 3.2. In vitro study

To assess the DAFF experimentally, magnetic silica particles (SiMAG-Silanol, 750 nm diameter; Chemicell GmbH, Berlin, Germany) were guided within a Y-shaped channel using the proposed dynamic magnetic actuation. A Y-shaped channel with a length of 5 mm and diameter of 1 mm, with equal stream flows in both outlets, is used to study guidance performance.

### 3.3. In vivo study

Fluorescent carboxyl magnetic particles Nile Red (FMNPs), 1% w/v (CATALOG NO: FCM-02556-2), were purchased from Spherotech (Libertyville, IL, USA). The NPs were 0.20–0.39 $\mu$m in diameter and were used in a previous study of drug delivery to the brain [27]. Nile Red is polymerized inside the core of the beads during the manufacturing process. In brief, the bead is polymerized in the first step with the Nile Red, magnetite, and styrene. The fluorescent tag is attached with NPs (FMNPs) and the excitation spectra of these FMNPs ranged from 400 to 500 nm,

and showed highly efficient fluorescence in the FITC channel at 488 nm when observed under a confocal laser scanning microscope (FLUOVIEW FV1000; Olympus, Tokyo, Japan), with an argon ion laser. The power of the laser was 20%. During the confocal microscopy experiment, we used DAPI dye to label the nuclei of the brain cells. To trace the FMNPs inside the mouse brain, the dye was attached to the magnetic particles before injecting them into the mouse, so there was no need for additional staining with the same dye to trace these particles inside the brain. The FMNPs were traced inside the brain with the help of the fluorescent molecules already attached to the magnetic particles; these were visible in the FITC channel at 488 nm (Figure. 11)

Male wild-type C57BL/6N mice (25–30 g, 8 weeks old) were purchased from Samtako Bio (Gyeonggi-do, South Korea). The mice were acclimatized for 1 week in the university animal house under a 12-h/12-h light/dark cycle at 23 °C and 60% humidity, and provided with food and water *ad libitum*. The mice were divided randomly into the following groups: A) DAFF(t), 6 A, $\alpha$ = 0.16, 0.144 Hz, B) FF(t), 6 A, 0.5 Hz, and C) Control. The mice in groups A and B received 0.4 mL of FMNPs via intravenous (i.v.) injection and were then exposed to the magnetic field for 10 minutes. The control animals were given 0.4 mL of 0.9% saline solution i.v. The mice were euthanized following the treatments. All efforts were made to minimize the number of mice used and their suffering. The experimental procedures were approved by the Animal Ethics Committee of the Division of Applied Life Sciences, Department of Biology, Gyeongsang National University, South Korea.

Brain tissues from all of the groups were collected after the treatments. Transcardial perfusion was performed with $1\times$ phosphate-buffered saline (PBS) followed by 4% ice cold paraformaldehyde. The brain tissues were post-fixed overnight in 4% paraformaldehyde and then transferred to 20% sucrose until they sank to the bottom of the tube. The brains were frozen in OCT (Tissue-Tek O.C.T. compound; Sakura Finetek USA, Torrance, CA, USA) and then cut into 14-$\mu$m sections in the coronal plane with a CM 3050S cryostat (Leica, Wetzlar, Germany). The sections were thaw-mounted on Probe-On positively charged slides (Thermo Fisher Scientific, Waltham, MA, USA) and stored at $-70$ °C.

The brain tissue slides were dried overnight and then washed twice with 0.01M PBS for 15 min each. The tissue sections were stained with DAPI for 10 min, rinsed with PBS, and glass coverslips were mounted on the slides with a fluorescent mounting medium. Images were captured using a confocal microscope (FLUOVIEW FV 1000; Olympus).

## 4. Conclusion

A novel magnetic field function design that can minimize aggregation effects was proposed. The proposed discontinuous asymmetrical field function was simulated by a computational platform to study targeting performance in a Y-shaped vessel. A discontinuous asymmetrical field function was designed to achieve guidance performance of 100%. Then, we showed experimentally that the proposed discontinuous asymmetrical field function can increase delivery performance via steering at the bifurcation *in vitro*. The size of aggregates is also reduced in comparison with FF. Furthermore, stationary aggregates are absent in the presence of a DAFF. *In vivo* experiments also revealed the effectiveness of DAFF in terms of BBB passage. Image analysis reveals that, compared with FF, DAFF results in the generation of smaller aggregates after passage of the BBB. DAFF (6 A, $\alpha$ = 0.16, 0.144 Hz) performed the best at BBB passage and drug uptake. The new actuation scheme, which was examined experimentally for MNP guidance and passage of the BBB, shows promising results. The mechanism of BBB passage, and determination of the optimum actuation function to enhance BBB passage, should be the subjects of future work.

**Author Contributions:** A.K.H. conceived and designed the study. A.K.H., T.L. and F.A.A. performed the experiments. A.K.H developed the simulation models, and wrote the manuscript. A.K.H., T.L., F.A.A., M.O.K., J.Y. Analyzed the data. All authors read and approved the manuscript.

384    **Conflicts of Interest:** The authors declare no conflict of interest.

385    **Bibliography**

386    1.    Hoshiar, A.; RaeisiFard, H.   A Simulation Algorithm for Path Planning of Biological Nanoparticles
387          Displacement on a Rough Path. *Journal of Nanoscience and Nanotechnology* **2017**, *17*, 5578–5581.
388    2.    Hoshiar, A.K.; Raeisifard, H.   A study of the nonlinear primary resonances of a micro-system under
389          electrostatic and piezoelectric excitations.   *Proceedings of the Institution of Mechanical Engineers, Part C:*
390          *Journal of Mechanical Engineering Science* **2015**, *229*, 1904–1917.
391    3.    Raeisifard, H.; Bahrami, M.N.; Yousefi-Koma, A.; Fard, H.R.   Static characterization and pull-in
392          voltage of a micro-switch under both electrostatic and piezoelectric excitations.   *European Journal of*
393          *Mechanics-A/Solids* **2014**, *44*, 116–124.
394    4.    Korayem, M.; Omidi, E. Robust controlled manipulation of nanoparticles using atomic force microscope.
395          *Micro & Nano Letters* **2012**, *7*, 927–931.
396    5.    Korayem, M.; Zakeri, M. Sensitivity analysis of nanoparticles pushing critical conditions in 2-D controlled
397          nanomanipulation based on AFM. *The International Journal of Advanced Manufacturing Technology* **2009**,
398          *41*, 714–726.
399    6.    Mekawy, M.; Saito, A.; Shimizu, H.; Tominaga, T.   Targeting of Apoptotic Cells Using Functionalized
400          Fe2O3 Nanoparticles. *Nanomaterials* **2015**, *5*, 874–884.
401    7.    Wang, S.; Meng, Y.; Li, C.; Qian, M.; Huang, R.   Receptor-Mediated Drug Delivery Systems Targeting to
402          Glioma. *Nanomaterials* **2016**, *6*.
403    8.    Dilnawaz, F.; Sahoo, S.K.   Therapeutic approaches of magnetic nanoparticles for the central nervous
404          system. *Drug Discovery Today* **2015**, *20*, 1256–1264.
405    9.    Merino, S.; Martín, C.; Kostarelos, K.; Prato, M.; Vázquez, E.   Nanocomposite Hydrogels:   3D
406          Polymer–Nanoparticle Synergies for On-Demand Drug Delivery. *ACS nano* **2015**, *9*, 4686–4697.
407    10.   Shityakov, S.; Roewer, N.; Broscheit, J.A.; Förster, C.   In silico models for nanotoxicity evaluation and
408          prediction at the blood-brain barrier level: A mini-review. *Computational Toxicology* **2017**, *2*, 20 – 27.
409    11.   Béduneau, A.; Saulnier, P.; Benoit, J.P. Active targeting of brain tumors using nanocarriers. *Biomaterials*
410          **2007**, *28*, 4947 – 4967.
411    12.   Arruebo, M.; Fernández-Pacheco, R.; Ibarra, M.R.; Santamaría, J.   Magnetic nanoparticles for drug
412          delivery. *Nano Today* **2007**, *2*, 22 – 32.
413    13.   Pankhurst, Q.A.; Thanh, N.T.K.; Jones, S.K.; Dobson, J. Progress in applications of magnetic nanoparticles
414          in biomedicine. *Journal of Physics D: Applied Physics* **2009**, *42*, 224001.
415    14.   Mosbach, K.; Schröder, U. Preparation and application of magnetic polymers for targeting of drugs. *FEBS*
416          *Letters* **1979**, *102*, 112 – 116.
417    15.   Kenjereš, S.; Righolt, B. Simulations of magnetic capturing of drug carriers in the brain vascular system.
418          *International Journal of Heat and Fluid Flow* **2012**, *35*, 68 – 75.
419    16.   Lunnoo, T.; Puangmali, T. Capture Efficiency of Biocompatible Magnetic Nanoparticles in Arterial Flow:
420          A Computer Simulation for Magnetic Drug Targeting. *Nanoscale Research Letters* **2015**, *10*, 426.
421    17.   Larimi, M.; Ramiar, A.; Ranjbar, A.   Numerical simulation of magnetic nanoparticles targeting in a
422          bifurcation vessel. *Journal of Magnetism and Magnetic Materials* **2014**, *362*, 58 – 71.
423    18.   Chertok, B.; David, A.E.; Yang, V.C.   Brain tumor targeting of magnetic nanoparticles for potential drug
424          delivery: Effect of administration route and magnetic field topography. *Journal of Controlled Release* **2011**,
425          *155*, 393 – 399.
426    19.   Tehrani, M.D.; Yoon, J. Statistical investigation of efficiency of the nanomagnetic particle steering in blood
427          vessels. The 7th IEEE International Conference on Nano/Molecular Medicine and Engineering, 2013, pp.
428          36–40.
429    20.   Mathieu, J.B.; Martel, S. Steering of aggregating magnetic microparticles using propulsion gradients coils
430          in an MRI Scanner. *Magnetic Resonance in Medicine* **2010**, *63*, 1336–1345.
431    21.   Kong, S.D.; Lee, J.; Ramachandran, S.; Eliceiri, B.P.; Shubayev, V.I.; Lal, R.; Jin, S.   Magnetic targeting of
432          nanoparticles across the intact blood–brain barrier. *Journal of Controlled Release* **2012**, *164*, 49 – 57.
433    22.   Bai, J.; Wang, J.T.W.; Mei, K.C.; Al-Jamal, W.T.; Al-Jamal, K.T.   Real-time monitoring of magnetic drug
434          targeting using fibered confocal fluorescence microscopy. *Journal of Controlled Release* **2016**, *244*, 240 – 246.

23. Ramaswamy, B.; Kulkarni, S.D.; Villar, P.S.; Smith, R.S.; Eberly, C.; Araneda, R.C.; Depireux, D.A.; Shapiro, B. Movement of magnetic nanoparticles in brain tissue: mechanisms and impact on normal neuronal function. *Nanomedicine: Nanotechnology, Biology and Medicine* **2015**, *11*, 1821 – 1829.

24. Tehrani, M.D.; Yoon, J.H.; Kim, M.O.; Yoon, J. A Novel Scheme for Nanoparticle Steering in Blood Vessels Using a Functionalized Magnetic Field. *IEEE Transactions on Biomedical Engineering* **2015**, *62*, 303–313.

25. Soheilian, R.; Choi, Y.S.; David, A.E.; Abdi, H.; Maloney, C.E.; Erb, R.M. Toward Accumulation of Magnetic Nanoparticles into Tissues of Small Porosity. *Langmuir* **2015**, *31*, 8267–8274.

26. Min, K.A.; Shin, M.C.; Yu, F.; Yang, M.; David, A.E.; Yang, V.C.; Rosania, G.R. Pulsed Magnetic Field Improves the Transport of Iron Oxide Nanoparticles through Cell Barriers. *ACS Nano* **2013**, *7*, 2161–2171.

27. Amin, F.U.; Hoshiar, A.K.; Do, T.D.; Noh, Y.; Shah, S.A.; Khan, M.S.; Yoon, J.; Kim, M.O. Osmotin-loaded magnetic nanoparticles with electromagnetic guidance for the treatment of Alzheimer's disease. *Nanoscale* **2017**, *9*, 10619–10632.

28. Morimoto, H.; Maekawa, T. Cluster structures and cluster-cluster aggregations in a two-dimensional ferromagnetic colloidal system. *Journal of Physics A: Mathematical and General* **2000**, *33*, 247.

29. Vartholomeos, P.; Mavroidis, C. Simulation platform for self-assembly structures in MRI-guided nanorobotic drug delivery systems. Robotics and Automation (ICRA), 2010 IEEE International Conference on. IEEE, 2010, pp. 5594–5600.

30. Vartholomeos, P.; Mavroidis, C. In silico studies of magnetic microparticle aggregations in fluid environments for MRI-guided drug delivery. *Biomedical Engineering, IEEE Transactions on* **2012**, *59*, 3028–3038.

31. Hoshiar, A.K.; Le, T.A.; Amin, F.U.; Kim, M.O.; Yoon, J. Studies of aggregated nanoparticles steering during magnetic-guided drug delivery in the blood vessels. *Journal of Magnetism and Magnetic Materials* **2017**, *427*, 181 – 187.

32. Li, S.; Marshall, J.S.; Liu, G.; Yao, Q. Adhesive particulate flow: The discrete-element method and its application in energy and environmental engineering. *Progress in Energy and Combustion Science* **2011**, *37*, 633–668.

33. Le, T.A.; Hoshiar, A.K.; Do, T.D.; Yoon, J. A modified functionalized magnetic Field for nanoparticle guidance in magnetic drug targeting. 2016 13th International Conference on Ubiquitous Robots and Ambient Intelligence (URAI), 2016, pp. 493–496.

34. Do, T.D.; Amin, F.U.; Noh, Y.; Kim, M.O.; Yoon, J. Guidance of Magnetic Nanocontainers for Treating Alzheimer's Disease Using an Electromagnetic, Targeted Drug-Delivery Actuator. *Journal of Biomedical Nanotechnology* **2016**, *12*, 569–574.

35. Hassan, S.; Yoon, J. Nano carriers based targeted drug delivery path planning using hybrid particle swarm optimizer and artificial magnetic fields. 2012 12th International Conference on Control, Automation and Systems, 2012, pp. 1700–1705.

36. Hoshiar, A.K.; Le, T.A.; Amin, F.U.; Kim, M.O.; Yoon, J. Functionalized Electromagnetic Actuation Method for Aggregated Nanoparticles Steering. International Conference of the IEEE Engineering in Medicine and Biology Society (EMBC). IEEE, 2017, pp. 885–888.

37. Kong, S.D.; Lee, J.; Ramachandran, S.; Eliceiri, B.P.; Shubayev, V.I.; Lal, R.; Jin, S. Magnetic targeting of nanoparticles across the intact blood–brain barrier. *Journal of controlled release* **2012**, *164*, 49–57.

38. Bae, J.E.; Huh, M.I.; Ryu, B.K.; Do, J.Y.; Jin, S.U.; Moon, M.J.; Jung, J.C.; Chang, Y.; Kim, E.; Chi, S.G.; others. The effect of static magnetic fields on the aggregation and cytotoxicity of magnetic nanoparticles. *Biomaterials* **2011**, *32*, 9401–9414.

39. Malvindi, M.A.; De Matteis, V.; Galeone, A.; Brunetti, V.; Anyfantis, G.C.; Athanassiou, A.; Cingolani, R.; Pompa, P.P. Toxicity assessment of silica coated iron oxide nanoparticles and biocompatibility improvement by surface engineering. *PloS one* **2014**, *9*, e85835.